

PULSED ACCRETION ONTO ECCENTRIC AND CIRCULAR BINARIES

DIEGO J. MUÑOZ AND DONG LAI

Cornell Center for Astrophysics and Planetary Science, Department of Astronomy, Cornell University, Ithaca, NY 14853, USA
Draft version April 4, 2016

ABSTRACT

We present numerical simulations of circumbinary accretion onto eccentric and circular binaries using the moving-mesh code AREPO. This is the first set of simulations to tackle the problem of binary accretion using a finite-volume scheme on a freely moving mesh, which allows for accurate measurements of accretion onto individual stars for arbitrary binary eccentricity. While accretion onto a circular binary shows bursts with period of ~ 5 times the binary period P_b , accretion onto an eccentric binary is predominantly modulated at the period $\sim 1P_b$. For an equal-mass circular binary, the accretion rates onto individual stars are quite similar to each other, following the same variable pattern in time. By contrast, for eccentric binaries, one of the stars can accrete at a rate 10-20 times larger than its companion. This “symmetry breaking” between the stars, however, alternates over timescales of order $200P_b$, and can be attributed to a slowly precessing, eccentric circumbinary disk. Over longer timescales, the net accretion rates onto individual stars are the same, reaching a quasi-steady state with the circumbinary disk. These results have important implications for the accretion behavior of binary T-Tauri stars and supermassive binary black holes.

Subject headings: accretion, accretion disks – binaries: general – stars: pre-main sequence

1. INTRODUCTION

Spectroscopic T-Tauri star binaries can exhibit quasi-periodic photometric oscillations known as “pulsed accretion” (Jensen et al. 2007; Muzerolle et al. 2013; Bary & Petersen 2014). This variability is believed to arise from the complex accretion streams delivered onto the young stars from a tidally truncated circumbinary disk (e.g. Artymowicz & Lubow 1996). Similar circumbinary disks may also exist around supermassive binary black holes (SMBBHs), but the short periods of binary T-Tauri stars (BTTSs) offer an unparalleled coverage of the time-domain as the system can evolve over several orbits during observations and even up to hundreds of orbits between different observing campaigns. This makes BTTS ideal laboratories for circumbinary accretion physics, with direct implications for binary star and circumbinary planet formation, and with applications that extend to SMBBHs.

The complexity of circumbinary accretion flow requires direct hydrodynamical simulations. Several computational approaches have been taken to address this problem (Artymowicz & Lubow 1996; Günther & Kley 2002; MacFadyen & Milosavljević 2008; Cuadra et al. 2009; Hanawa et al. 2010; de Val-Borro et al. 2011; Roedig et al. 2012; Shi et al. 2012; D’Orazio et al. 2013; Pelupessy & Portegies Zwart 2013; Farris et al. 2014; Lines et al. 2015), ranging from Lagrangian methods to Eulerian ones on polar and cartesian grids. Of these, only a subset has been able to simulate the accretion flow onto the individual stars, or to include eccentricity in the binaries; only two studies have attempted both (Günther & Kley 2002; de Val-Borro et al. 2011).

Considering eccentric binaries in simulations is essential for pulsed accretion, as accretion luminosity is likely to depend on the orbital phase (Basri et al. 1997; Huerta et al. 2005; Jensen et al. 2007; Bary et al. 2008). Although high eccentricities in BTTSs are common – the binaries AK Sco, DQ Tau and UZ Tau E have eccentricities of $e_b=0.47$, 0.56 and 0.29 respectively (Andersen et al. 1989; Mathieu et al. 1997; Prato et al. 2002) – accurate simulation of circumbi-

nary accretion onto eccentric pairs remains a challenge. In this work, we present the first simulation results of circumbinary accretion using the moving-mesh code AREPO (Springel 2010). Unlike other implementations of finite-volume or finite-difference schemes for computational gas dynamics, the accuracy of AREPO does not depend on the value of e_b , as its space-discretization strategy is carried out via an unstructured mesh that moves with the local velocity of the flow. Thus, being a quasi-Lagrangian method, AREPO can naturally concentrate the resolution around the individual stars, resolving circum-single disks to good accuracy.

2. NUMERICAL METHODS

2.1. Moving-mesh Hydrodynamics

We run two-dimensional, non-selfgravitating hydrodynamic simulations of viscous circumbinary accretion disks (CBD) using AREPO with a time-explicit integration scheme for the Navier-Stokes terms (Muñoz et al. 2013). The computational domain is divided into Voronoi cells, distributed in a quasi-polar fashion (with 600 azimuthal zones) with logarithmic spacing in radius, following the accretion disk setup of Muñoz et al. (2014). Cells initially cover the radial range between $R = a_b(1 + e_b)$ to $R = R_{\text{out}} = 70a_b$ (where a_b is the binary semimajor axis) but are allowed to viscously evolve toward $R = 0$. At R_{out} , we impose inflow boundary conditions of steady accretion \dot{M}_0 , assuming that at these distances the disk is axisymmetric and the central potential Keplerian¹. The binary is represented by a prescribed rotating potential:

$$\Phi(\mathbf{r}) = -\mathcal{G}M_b \left[\frac{(1+q_b)^{-1}}{|\mathbf{r}-\mathbf{r}_1|} + \frac{q_b(1+q_b)^{-1}}{|\mathbf{r}-\mathbf{r}_2|} \right] \quad (1)$$

where $q_b = M_2/M_1$ is the binary mass ratio and $M_b = M_1 + M_2$ is the total mass. The individual stellar positions are $\mathbf{r}_1(t) = q(1+q)^{-1}\mathbf{r}(t)$ and $\mathbf{r}_2(t) = -(1+q)^{-1}\mathbf{r}(t)$ where the relative po-

¹ Radial inflow and axisymmetry are imposed by using a moving boundary and a narrow wave-absorbing region (as described in Muñoz et al. 2014) between $65a_b$ and $70a_b$.

sition vector $\mathbf{r}(t) = a_b(\cos E - e_b, (1 - e_b^2)^{1/2} \sin E)$. The eccentric anomaly $E(t)$ is obtained by solving Kepler's equation (e.g. Danby 1988). The potential around each star is softened²; the softening length is set to $s = 0.025a_b$.

The binary components are allowed to “accrete” (although their dynamical masses are held constant). Gas is drained from cells located within a distance of $r_{\text{acc}} = 0.8s = 0.02a_b$ from each star. The draining is carried out as a simple “open-boundary” condition, meaning that cells that are located within the accretion region are instantaneously drained³ (Muñoz et al. 2015). The accreted mass M_i is stored at every major time-step and accretion rates \dot{M}_1 and \dot{M}_2 are computed by central-difference differentiation of $M_i(t)$. Note that, for BTTSs with semi-major axis $a_b \sim 0.2$ AU (Jensen et al. 2007), we have $r_{\text{acc}} \sim 0.004$ AU $< 1R_\odot$, sufficient to resolve the accretion down to the stellar surface. On the other hand, for a SMBBH, the “true” accretion radius (e.g., the innermost stable circular orbit) is $\ll r_{\text{acc}}$, and the value of \dot{M}_i should be interpreted with caution (see Section 3.4 below).

As the outer CBD evolves, resolution is maintained roughly constant via de-refinement and refinement operations (Springel 2010). Within $R = a_b(1 + e_b)$, the resolution criterion is switched over from “volume-based” to “mass-based”, in which there is a “target mass” m_{gas} enforced for all cells (Springel 2010). The transition between mass-based and volume-based resolution is kept smooth by controlling the volume difference between contiguous cells (Pakmor et al. 2013). For our lowest-resolution runs, $m_{\text{gas}} = 6.3 \times 10^{-7} \Sigma_0 a_b^2$, where Σ_0 is the scaling of the initial disk surface density profile (see Section 2.2 below). In this region, there is a minimum permitted volume, $\pi s^2/20$, where s is the softening parameter.

The equation of state is “locally isothermal”⁴: $P = \Sigma c_s(\mathbf{r})$, where the sound speed is a function of position only (e.g. Farris et al. 2014): $c_s^2(\mathbf{r}) = -h_0^2 \Phi(\mathbf{r})$, where the aspect ratio h_0 is a global constant. When $|\mathbf{r}| \gg |\mathbf{r}_1|, |\mathbf{r}_2|$, then $c_s^2 \approx h_0^2 \mathcal{G}M_b/|\mathbf{r}|$; and when $|\mathbf{r} - \mathbf{r}_i| \ll |\mathbf{r} - \mathbf{r}_j|$, then $c_s^2 \approx h_0^2 \mathcal{G}M_i/|\mathbf{r} - \mathbf{r}_i|$.

Finally, the kinematic viscosity ν follows an α -viscosity prescription (Shakura & Sunyaev 1973), in which $\nu = \alpha c_s^2 / \tilde{\Omega}(\mathbf{r})$. Where $\tilde{\Omega}(\mathbf{r})$ is a function that reduces to $(\mathcal{G}M_b/R^3)^{1/2}$ far from the binary, and to $(\mathcal{G}M_b/|\mathbf{r} - \mathbf{r}_i|)^{3/2}$ close to each star.

Throughout this work, we fix the parameters $q_b = 1$ and $h_0 = \alpha = 0.1$, while varying the binary eccentricity e_b .

2.2. Initial Setup

Knowing that the outer disk is in steady-state accretion, we “guess” an initial surface density profile $\Sigma(R)$ that includes a central cavity but that, at large radii, behaves as $\Sigma \propto \dot{M}_0/\nu \propto R^{-1/2}$. Thus, we adopt the initial CBD surface density profile:

$$\Sigma(R, t=0) = \Sigma_0 \left(\frac{R}{R_{\text{cav},0}} \right)^{-p} \exp \left[- \left(\frac{R}{R_{\text{cav},0}} \right)^{-\xi} \right], \quad (2)$$

where $p = 1/2$ and $R_{\text{cav},0}$ and ξ characterize the extent and steepness of the tidal cavity around the binary. In this work, we choose $R_{\text{cav},0} = 5a_b$ and $\xi = 4$. Steady-state at the onset of

² We use a cubic spline softening, as in Springel et al. (2001).

³ At each time-step, we extract some fraction η of the cell mass, where η is a weighting factor that is unity at $|\mathbf{r} - \mathbf{r}_i| = 0$ and decreases with distance from the accreting object.

⁴ This equation of state requires an isothermal (iterative or approximate) Riemann solver with varying sound speed computed at each cell interface (Muñoz et al. 2014).

the simulation⁵ is guaranteed for $R \gg R_{\text{cav},0}$ by construction, but Eq. 2 is still an imperfect initial condition at intermediate radii, and a long integration time may be needed to relax the initial conditions for *all* R .

The initial condition is completed by specifying a rotation curve

$$\Omega^2 = \frac{\mathcal{G}M_b}{R^3} \left[1 + \frac{3}{4} \left(\frac{a_b}{R} \right)^2 \frac{q_b}{(1+q_b)^2} \left(1 + \frac{3}{2} e_b^2 \right) \right] + \frac{1}{R\Sigma} \frac{dP}{dR}, \quad (3)$$

which includes the quadrupole component of the potential and the contribution of the pressure gradient, and by specifying a radial velocity profile $v_R(R)$. Assuming a standard thin accretion disk, we impose

$$v_R = \frac{1}{R\Sigma} \frac{\partial}{\partial R} \left(\nu \Sigma R^3 \frac{d\Omega}{dR} \right) \left[\frac{d}{dR} (R^2 \Omega) \right]^{-1}, \quad (4)$$

which in turn specifies the accretion rate profile

$$\dot{M}(R) = -2\pi R v_R(R) \Sigma(R). \quad (5)$$

Note that this initial $\dot{M}(R)$ starts converging toward \dot{M}_0 only beyond $R \gtrsim 20a_b$ (at $t=0$, \dot{M} equals $1.41\dot{M}_0$ and $1.08\dot{M}_0$ at $R=10a_b$ and $15a_b$, respectively), and thus the disk is not started with a strictly steady accretion profile. Unless stated otherwise, we initially evolve the system for $2000P_b$ (where P_b is the binary orbital period), and study the subsequent evolution for an additional 600 binary orbits. This initial integration time corresponds to two viscous times at $6a_b$ or ten at $2a_b$, where the viscous time t_ν is defined for $\nu \propto R^{1/2}$ (Lynden-Bell & Pringle 1974) as

$$t_\nu = \frac{4R^2}{9\nu} = \frac{2P_b}{9\pi\alpha h_0^2} \left(\frac{R}{a_b} \right)^{3/2}. \quad (6)$$

For 1950 orbits, we evolve the disk using an open (diode-like) boundary on a set of controlled cells placed on a ring at $R_{\text{in}} = a_b(1 + e_b)$ ⁶. At $t = 1950P_b$, boundary cells are “released”, allowing them to fill in the cavity and form accretion disks around the individual stars. At $t \gtrsim 2000P_b$, we expect the CBD within $5a_b$ to be (on average) fully relaxed. We aim to reach a “relaxed state” inside the cavity as well, for which $\langle \dot{M}_1 + \dot{M}_2 \rangle_T \approx \langle \dot{M}(R) \rangle_T \approx \text{constant}$ for a wide range in R , after averaging over some time interval T . The outer disk ($R \gtrsim 40a_b$) is in steady-state by construction. However, there is an intermediate region, with $t_\nu \gg 2000P_b$, that has had no time yet to relax (see below).

2.3. Long-term Disk Relaxation

Inspection of the initial condition reveals that $\dot{M}(R, t=0)$ coincides with \dot{M}_0 to within 1% only for $R > 42a_b$. This is just an artifact of the initial condition. To guarantee $\dot{M}(R) \approx \dot{M}_0$ across all radii, we would need to evolve the system for $\sim 20000P_b$ (or t_ν at $40a_b$; Eq. 6), a daunting task for the simulation work presented here. Instead, after some integration time t_{int} , the system has only reached relaxation within a “relaxation radius” $R_{\text{rel}} \equiv a_b [(9/2)\pi\alpha h_0^2 (t_{\text{int}}/P_b)]^{2/3}$ (from setting $t_{\text{int}} = t_\nu(R_{\text{rel}})$ in Eq. 6; see Rafikov 2016). After $t = 2000P_b$,

⁵ Imposing $\Sigma \propto \dot{M}_0/\nu \propto R^{-1/2}$ in the outskirts of the disk is essential for a steady-state solution to exist, and the only way to meaningfully compare binary accretion rates to those of single point masses (see Rafikov 2016 for a similar argument).

⁶ An open boundary consists of a collection of cells with a prescribed motion playing the role of “ghost cells” with outflow boundary conditions (Muñoz et al. 2013; Muñoz et al. 2014).

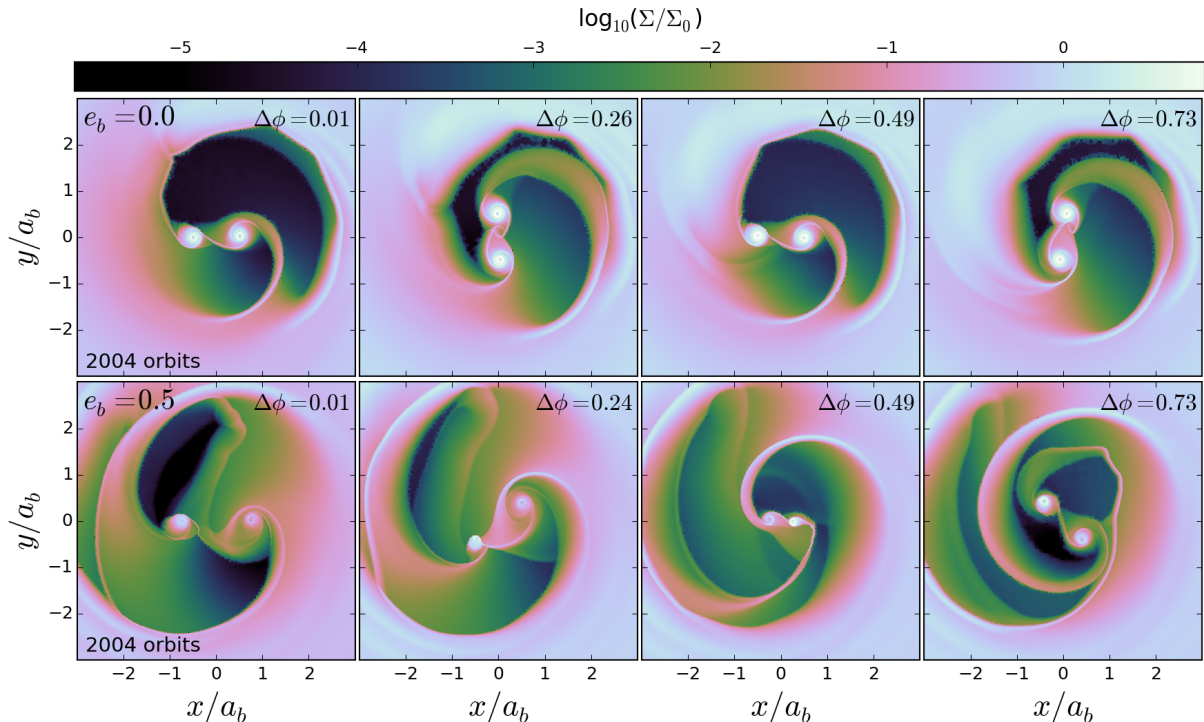


Figure 1. Surface density field evolution within timescales of ~ 1 binary orbit for circular (top panels) and eccentric (bottom panels) binaries at $2004 + \Delta\phi$ binary orbits (where the relative phase $\Delta\phi \approx 0, 0.25, 0.5, 0.75$ is measured since the last apocenter). For the $e_b = 0$ case, the pattern repeats every half orbit. By contrast, in the $e_b = 0.5$ case, there is a noticeable asymmetry in the density field. Since $q_b = 1$, the asymmetry cannot depend on the binary properties, but must be imposed by the way gas is funneled into the central cavity. An eccentric inner disk could favor one star over the other. Note that the accretion rate asymmetry is reversed after several binary orbits (see Section 3.3) and Fig. 3).

$R_{\text{rel}} \approx 9.3a_b$, which is $\ll 42a_b$, but sufficiently large for the disk to be nearly axisymmetric outside that radius. Without reaching global relaxation, we have found that the disk within R_{rel} receives a gas supply from the partially relaxed portion of the disk ($R_{\text{rel}} \lesssim R \lesssim 2R_{\text{rel}}$) at a rate \dot{M}_{out} slightly larger (by about 10%) than \dot{M}_0 , as a result of the initial condition⁷. This accretion “excess” cannot not be removed with only 2000 orbits of integration time.

3. SIMULATION RESULTS

3.1. Accretion Flows in the Circumbinary Cavity

Figure 1 shows several snapshots of the density field for accretion onto a circular binary (top) and an eccentric one (bottom). The tidal “cavity” around the binary is asymmetric and non-circular, making it difficult to identify an unambiguous cavity “radius”. Within the cavity, flow is complex and transient, dominated by accretion streams, which show significantly more structure (and unsteadiness) in the eccentric case. In the circular case, the “streamers” rotate with the binary, while this is not the case when $e_b \neq 0$. Similarly, the cavity shape and contrast nearly repeats itself every half orbit when $e_b = 0$, while no such symmetry is observed when $e_b = 0.5$.

The symmetries of the $e_b = 0$ case are also evident from the properties of the circumbinary disks (CSDs): both CSDs are similar in size, density and morphology (including $m = 2$ spiral patterns in each). By contrast, the CSDs in the $e_b = 0.5$ case show differences in surface density, implying that the mem-

⁷ The annulus that supplies gas to the inner CBD can be roughly estimated by integrating the traveled distance from $R_{\text{out,eff}}$ down to a R_{rel} at a velocity of $v_R \sim -\frac{3}{5}\nu/R = -\frac{3}{5}\alpha h^2 a_b \Omega_b (R/a_b)^{-1/2}$, giving $(R_{\text{out,eff}}/a_b)^{3/2} = 9\pi\alpha h_0^2 (t_{\text{int}}/P_b)$ or $R_{\text{out,eff}} = 2^{2/3} R_{\text{rel}} \approx 14.7a_b$ if $t_{\text{int}} = 2000P_b$. From Eqs. (2) and (5), we have $\dot{M}(R = 14.7a_b, t = 0) \approx 1.1\dot{M}_0$.

bers of the equal-mass binary accrete at different rates. We will further address this “disk disparity” in Section 3.3 below.

3.2. Accretion rates

A schematic description of the circumbinary accretion process is the following: there are three accretion disks – the CBD and the two CSDs – that evolve viscously, but are connected via fast accretion bursts owing to the (unstable) tidal streams launched at the inner edge of the CBD. If $e_b \neq 0$, the outer edges of the CSDs collect new material at apocenter, when the accreting masses are closest to the CBD inner edge. Subsequently, the incoming material is viscously transported inward within the CSD, eventually accreting onto the stars at some later phase in the orbit. The (presumably) much slower rate at which material is transported onto the accreting objects relative to fast deposition of material to the outer edge of the CSDs turns the CSDs into “buffers”. The buffers damp the fast oscillations in \dot{M} present in the circumbinary cavity before they reach the stars.

Although compelling, this idealized depiction is clearly too simplistic in the light of the simulations results of Fig. 1. We compute $\dot{M}(R)$ (Eq. 5) at different radii⁸ of the CBD. Figure 2 shows $\dot{M}(R)$ at $R = (1 + e_b), 3, 5, 7$ and $10 \times a_b$ as a function of time for $e_b = 0$ (left) and $e_b = 0.5$ (right). In particular, $R = a_b(1 + e_b)$ is where the innermost boundary would be located in a polar-grid simulation. The total accretion onto the central masses $\dot{M}_{\text{bin}} \equiv \dot{M}_1 + \dot{M}_2$ is shown on top. Accretion rates are normalized to a reference value \dot{M}_{out} , which is the accretion rate at a radius where the disk becomes axisymmetric. We measure the mean $\langle \dot{M} \rangle_T$ over a period $T = 60P_b$ in each

⁸ We compute $\dot{M}(R, \phi) = 2\pi R v_R(R, \phi) \Sigma(R, \phi)$ for all Voronoi cells in the vicinity of radius R and then take an azimuthal average.

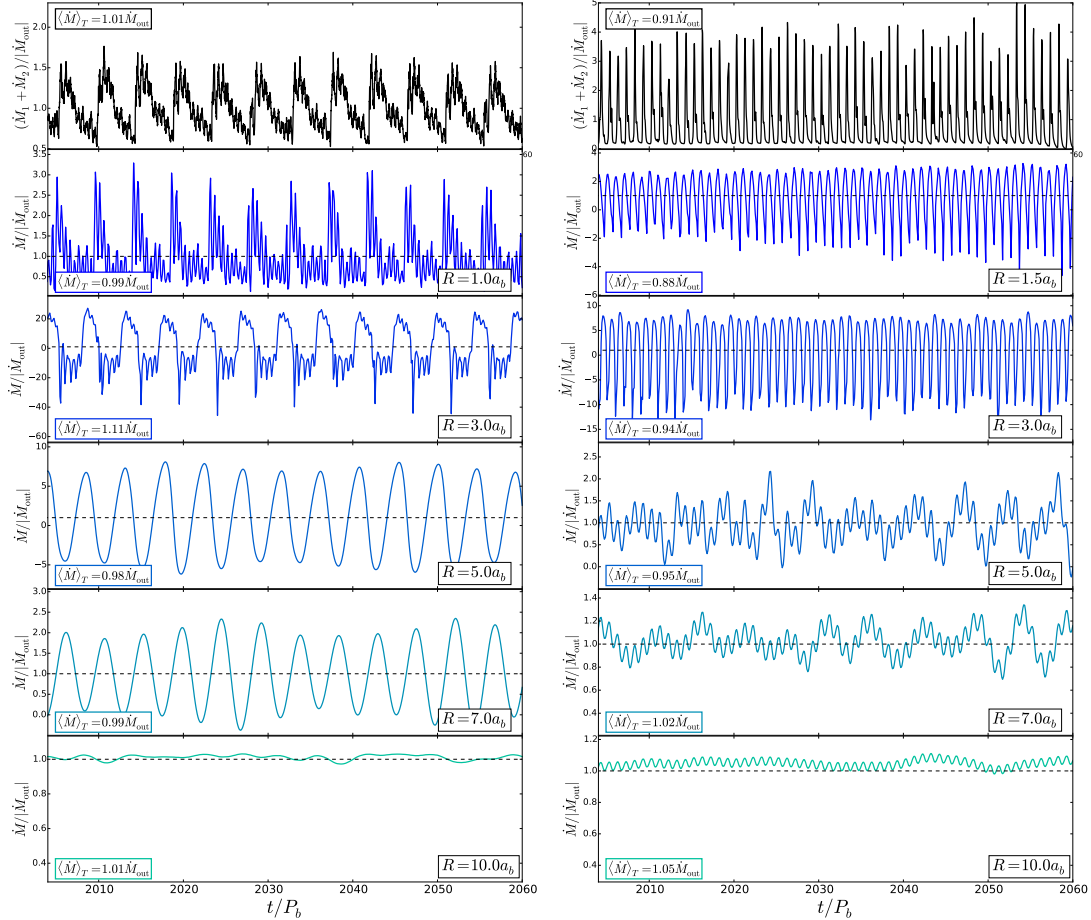


Figure 2. Accretion rate as a function of time over short time scales ($T = 60P_b$) at different radii in the disk. From top to bottom, total accretion rate onto the binary ($\dot{M}_1 + \dot{M}_2$) followed by accretion rate ($\dot{M} = -2\pi R v_R \Sigma$) at $R = a_b(1 + e_b)$, $3a_b$, $5a_b$, $7a_b$ and $10a_b$. The left panels are for $e_b = 0$ and the right panels for $e_b = 0.5$. Values are normalized by \dot{M}_{out} (represented by the black dashed line), which is obtained by identifying the smallest radius at which the RMS time variability of \dot{M} is less than 1% (a proxy for axisymmetry) and assigning $\dot{M}_{\text{out}} = \langle \dot{M} \rangle_T$ at that radius. For the $e_b = 0$ case, this radius is identified to be $\approx 11a_b$, and for the $e_b = 0.5$ case, it is $\approx 15a_b$. In both cases $\dot{M}_{\text{out}} \approx 1.19M_0$. Variability of \dot{M} in the inner region ($R < 3a_b$) has a dominant period of $5P_b$ in the case of $e_b = 0$ and $\sim 1P_b$ in the case of $e_b = 0.5$. The averaged \dot{M} over $T = 60P_b$ is close to but not exactly \dot{M}_{out} , implying that there is variability on timescales longer than shown here. Note that accretion rates at a distance of $a_b(1 + e_b)$ – where an open boundary condition would be imposed in polar-grid simulations – are always positive for $e_b = 0$ but alternate sign when $e_b = 0.5$; the latter that cannot be captured by an open boundary. This is in consistency with the appearance of shocks inside the cavity (Fig. 1) as a result of the convergence of inflowing and outflowing streams.

panel (see figure caption). In the $e_b = 0$ case (Fig. 2, left panels), there is a clear accretion modulation with period $\sim 5P_b$ (roughly the Keplerian period at $R = 3a_b$), observed in \dot{M}_{bin} (top panel) as well as in the CBD out to $R = 7a_b$. Right at the putative edge of the CBD disk ($\approx 3a_b$), the evolution of \dot{M} turns significantly more complex (a quasi-periodicity of $5P_b$ is still present), and extremely variable in amplitude (going from -40 to $+20 \dot{M}_{\text{out}}$). For $R < 3a_b$, modulation of \dot{M} is dominated by a $1P_b$ component superposed to major bursts that repeat every $\sim 5P_b$. This bursty accretion has been seen in previous numerical experiments (D’Orazio et al. 2013; Farris et al. 2014), being attributed to an over-dense “lump” that forms at the rim of the cavity, and gets periodically “flung” onto the binary (see Fig. 1, top panels). Note that at $R = 1a_b$ – where a polar-grid code would place the outflow computational boundary – \dot{M} is always positive, and thus artifacts introduced by diode-like boundary conditions (not allowing for material with $v_R > 0$ to enter the domain) are minimal. The two top panels of Fig. 2 show good qualitative agreement with each other, the differences being (1) a delay in the time of the accretion burst to reach the stars, and (2) a reduction of the amplitude of the variability; these differences are consistent

with the buffering nature of a viscous disk.

The $e_b = 0.5$ case (Fig. 2, right panels) shows much more complex \dot{M} variability outside $R = 3a_b$. By contrast, for $R < 3a_b$, variability seems simpler than around a circular binary. In particular, $\sim 1P_b$ is the dominant modulation period, although trends of periods longer than $60P_b$ are also noticeable. The amplitude of the oscillations in \dot{M}_{bin} (Fig. 2, top right panel) can be as high as $5\dot{M}_{\text{out}}$ in contrast with $\sim 1.5\dot{M}_{\text{out}}$ for the $e_b = 0$ case. Another striking difference from the $e_b = 0$ case is the value of \dot{M} around the binary. The imaginary boundary at $R = a_b(1 + e_b)$ (second right panel from top) shows alternating negative and positive values in \dot{M} . Evidently, a diode-like boundary placed at $R = a_b(1 + e_b)$ could not capture this sign-changing behavior.

3.3. Individual Accretion Rates and Correlation with Periastron Separation

In Fig. 3 we show accretion onto the individual stars \dot{M}_1 and \dot{M}_2 over 160 binary orbits. For the $e_b = 0$ case (left panels), the symmetry between the primary and secondary is remarkable, as it is expected for $q_b = 1$. This is at odds with the results of Farris et al. (2014) which shows a mild “symmetry breaking” in \dot{M}_i . Both \dot{M}_1 and \dot{M}_2 show the bursty nature of the

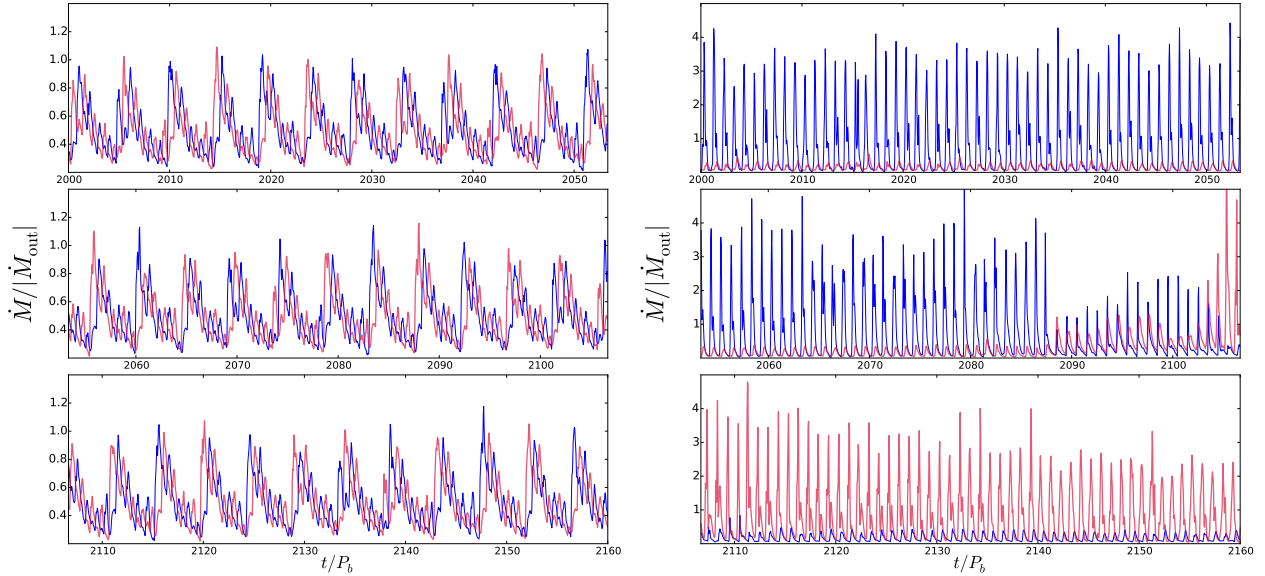


Figure 3. Accretion rate onto the primary and secondary members of the binary, \dot{M}_1 and \dot{M}_2 in blue and red respectively, for eccentricities $e_b=0$ (left) and $e_b=0.5$ (right). Each column spans the range from 2000 to $2160P_b$ out of a longer integration period ending at $2600P_b$. Values are normalized by \dot{M}_{out} . The eccentric binary shows a strong modulation of its accretion rate at the binary orbital period, although long-term trends are also present. The circular binary shows strong modulation at both $\sim 1P_b$ and $\sim 5P_b$ (as observed also by D’Orazio et al. 2013 and Farris et al. 2014) and longer-term trends are less obvious than in the eccentric case. The eccentric binary experiences a symmetry breaking, with one star accreting between 10 and 20 times more mass than its companion. This trend, however, is reversed at $t \sim 2100P_b$ and then reversed back at $t \sim 2300P_b$ (not shown). In the long term (600 orbits), the average accretion rates are $\langle \dot{M}_1 \rangle_{600} = 0.5\dot{M}_{\text{out}}$ and $\langle \dot{M}_2 \rangle_{600} = 0.5\dot{M}_{\text{out}}$ for the circular binary, and $\langle \dot{M}_1 \rangle_{600} = 0.48\dot{M}_{\text{out}}$ and $\langle \dot{M}_2 \rangle_{600} = 0.51\dot{M}_{\text{out}}$ for the eccentric binary.

two top left panels of Fig. 2, although they do not perfectly lie on top of each other; instead, one star undergoes an accretion burst before its companion. The lag between the two bursts is about a half orbit, although the sign of the lag alternates on each major burst.

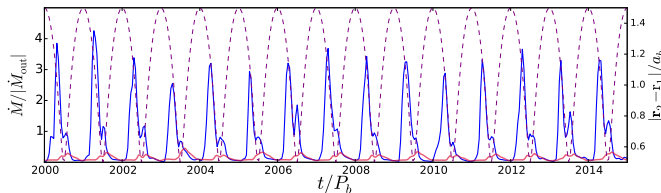


Figure 4. Individual accretion rates for the primary (blue) and secondary (red) in the $e_b=0.5$ case over an interval of 15 orbits contrasted to orbital separation (purple dashed curve). The primary (only temporarily dominating the accretion rate, Fig. 3) shows a double peaked behavior, with a dominant peak consistently located at an orbital phase of $\phi = -0.2$ (relative to time of pericenter) and a minor peak immediately after/during pericenter. The secondary also shows a double peaked accretion curve (immediately before and after pericenter), although with comparable amplitudes.

For $e_b=0.5$ (right panels of Fig. 3), the symmetry breaking between \dot{M}_1 and \dot{M}_2 is evident. Despite the having $q_b = 1$, over the first ~ 90 orbits, \dot{M}_1 (blue) is 10-20 times larger than \dot{M}_2 (red). Interestingly, after 100 orbits, this behavior switches to $\dot{M}_2 \gg \dot{M}_1$, only to switch back to $\dot{M}_1 \gg \dot{M}_2$ at $t = 2300P_b$ (not shown). Over timescales of $\sim 600P_b$, we have that $\dot{M}_1 \approx \dot{M}_2$, recovering – in a time-averaged sense – the symmetry that is to be expected when $q_b = 1$. The reason for this dramatic difference between \dot{M}_1 and \dot{M}_2 must originate in a symmetry breaking in the CBD itself. If the CBD is eccentric, the relative longitude of pericenter $\varpi_d - \varpi_b$ (where $\varpi_d(R)$ specifies the orientation of a given elliptical portion of the CBD disk) will determine the timing of mass transfer from the CBD to the binary. In principle, an eccentric disk should precess around the binary at a rate $\dot{\varpi}_d$, implying that, if one of the accreting objects is benefited by an increased \dot{M} at any given

time, at some later time preferential accretion should be reversed. A relevant precession rate is that of the inner rim of the CBD, at a radius of $R_{\text{cav}} \sim 2 - 3a_b$. In the limit of a pressure-less particle disk, the precession rate around an eccentric binary is

$$\dot{\varpi}_d \simeq \frac{3\Omega_b}{4} \frac{q_b}{(1+q_b)^2} \left(1 + \frac{3}{2}e_b^2\right) \left(\frac{a_b}{R}\right)^{7/2} \sim 0.006\Omega_b \left(\frac{3a_b}{R}\right)^{7/2}, \quad (7)$$

which corresponds to precession period of a few hundred P_b at $R \sim 3a_b$. This precession period roughly coincides with the period of alternation of dominant accretion shown in Fig. 3. Future work will take deeper look into the properties of precessing eccentric CBDs (Miranda, Muñoz & Lai, in prep).

In Fig. 4, we show a portion of Fig. 3 ($e_b=0.5$ case, right panels) overlaid with the binary separation $|\mathbf{r}_2 - \mathbf{r}_1|$. In the case where \dot{M}_{bin} is dominated by \dot{M}_1 (blue curve) accretion peaks before pericenter passage, exhibiting a minor second peak exactly at pericenter. This is in partial agreement the simulation results of Günther & Kley (2002) and de Val-Borro et al. (2011), although the accretion burst peaks noticeably before pericenter, and the burst duration spans a significant fraction of the orbital period.

3.4. Tidal Torques and the Effect of Increased Resolution

We now examine the buffering nature of the CSD discussed above (Section 3.2). When the accretion radius r_{acc} (Section 2.1) is much smaller than the size of the CSD R_{cs1} , the accretion time $t_{\text{acc,cs1}}$ within a CSD is roughly the viscous time at the disk edge⁹ $t_{\nu,\text{cs1}} = 2P_b / (9\pi\alpha h_0^2) (R_{\text{cs1}}/a_b)^{3/2} \sqrt{1+q_b}$. This timescale enables the damping of fast modulations and sets a delay between the time of gas deposition onto the CSD

⁹ If the condition $r_{\text{acc}} \ll R_{\text{cs1}}$ is not satisfied, a more general expression for the accretion time is $t_{\text{acc,cs1}} = t_{\nu,\text{cs1}} [1 - (r_{\text{acc}}/R_{\text{cs1}})^{3/2}]$.

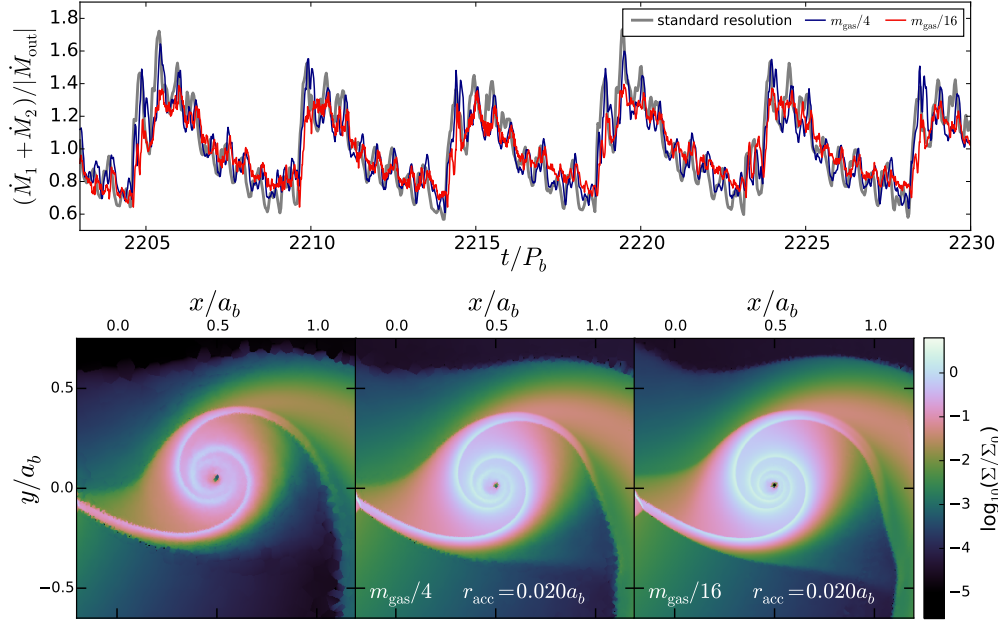


Figure 5. Top panels: density field around the primary at $t = 2220P_b$ for a resolution mass of $m_{\text{gas}} = 6.3 \times 10^{-7} \Sigma_0 a_b^2$ (left), $m_{\text{gas}}/4$ (center) and $m_{\text{gas}}/16$ (right). In all cases $r_{\text{acc}} = 0.02a_b$ (Section 3.4). Bottom panel: stellar accretion \dot{M}_{bin} as a function of time for the three different mass resolutions. Both the burst in accretion with period $\sim 5P_b$ and the high-frequency modulations with periods $\lesssim 1P_b$ are prevalent at all different resolutions, strengthening the hypothesis that the prominent $m=2$ features drive the accretion onto the stars. When the same experiment is run after decreasing $r_{\text{acc}} = 0.02a_b$ and s (by a factor of 2 and then by a factor of 4) in addition to m_{gas} (by a factor of 4 and 16 respectively), the long term modulation of the accretion rate persists, but the high frequency component is progressively washed away. This, again, is consistent with transport via resonant torques, as for r_{acc} sufficiently small, the tidal forcing from the secondary becomes negligible (Eq. 9).

and the time of actual accretion onto the stars. With an estimate of R_{cs1} ¹⁰, we have $t_{\nu, \text{cs1}} \approx 23P_b$. This time may be short enough to enable the accretion burst of period $\sim 5P_b$ to reach the stars, but it is perhaps too long to allow for the persistence of the high frequency oscillations (periods $\sim 1P_b$ and shorter; Figs. 2 and 3, left panels). However, the fast oscillations in \dot{M}_{bin} might be explained by mass transport via tidal torques. In a circum-primary frame (primed coordinates), the potential on the CSD due to the secondary is (e.g., Miranda & Lai 2015)

$$\Phi_{\text{sec}}(\mathbf{r}') \approx \mathcal{G} M_b \frac{q_b}{1+q_b} \frac{1}{4} \left(\frac{r'}{a_b} \right)^2 [1 + 3 \cos(2\Omega_b t)] \quad (9)$$

where we have dropped a constant term. The time-dependent term can excite $m=2$ modes in the density field of the circum-primary disk (Fig. 1), which may explain the high-frequency modulation of \dot{M}_{bin} as the spiral overdensities move into the accretion region. Note that our accretion routine is somewhat resolution-dependent (cells are drained depending on their location, regardless of their total mass content; see Muñoz et al. 2015). For a given \dot{M}_0 , the average number of cells being accreted in an interval Δt is $N_{\text{acc}} = (\dot{M}_0/m_{\text{gas}})\Delta t$, with a “signal-to-noise ratio”¹¹ of $\sqrt{N_{\text{acc}}} \approx 200\sqrt{\Omega_b \Delta t}$. For $\Delta t \sim 0.05P_b$, the uncertainty in the measured \dot{M}_{bin} is $\sim 1\%$, small enough to be confident in the general features of Fig. 3, but large enough to justify a convergence study of the high-frequency modulations (see Pakmor et al. 2016). Fig. 5 (top panels) shows the

¹⁰ We replace R_{cs1} with the Eggleton approximation of the Roche radius (Eggleton 1983):

$$(R_{\text{cs1}}/a_b) = 0.49q_b^{-2/3} / \left[0.6q_b^{-2/3} + \ln(1+q_b^{-1/3}) \right]. \quad (8)$$

¹¹ The imposed accretion rate \dot{M}_0 and mass resolution are related by $\dot{M}_0 = 3\sqrt{5}\pi\alpha h_0^2 (R_{\text{cav},0}/5a_b)^{1/2} [m_{\text{gas}}\Omega_b/(6.7 \times 10^{-3})]$.

circum-primary density field at three different gas resolutions (while keeping r_{acc} and the softening length s fixed), confirming the prevalence of $m=2$ spiral arms. The bottom panel of Fig. 5 shows \dot{M}_{bin} at the same three resolutions, confirming the major accretion burst, and that the rapid oscillations are real and likely a result of a time-dependent forcing (Eq. 9). Note that the strength of this forcing in Eq. 9 is negligible for $r' \ll a_b$; thus, one can expect the influence of the companion (and thus the high frequency modes of \dot{M}_{bin}) to be drastically reduced as r_{acc} is made smaller. We repeat the resolution experiments of Fig. 5 (not shown), this time decreasing r_{acc} and s in addition to m_{gas} . We find that the fast modulations are progressively damped out; and for very small r_{acc} , only the major accretion bump survives, as the accretion (buffering) time within the CSD is not long enough to entirely erase it.

4. SUMMARY AND IMPLICATIONS

We have presented two-dimensional, viscous flow simulations of circumbinary disk accretion for the first time using a finite-volume method on a freely moving Voronoi mesh. Previous simulations based on structured moving grids were restricted to circular binaries (e.g. Farris et al. 2014). Using AREPO, we can robustly simulate accretion onto arbitrarily eccentric binaries, without the constraints imposed by structured grids. In our simulations, we are able to follow the mass accretion through a wide radial extent of the circumbinary disk, leading to accretion onto individual members of the binary via circumstellar disks.

Our simulations have revealed dramatic differences between the accretion behavior of circular and eccentric binaries:

(1) In agreement with previous studies (e.g. D’Orazio et al. 2013; Farris et al. 2014), we find that accretion onto equal-mass, circular binaries exhibits quasi-periodic variabilities with a dominant period of $\sim 5P_b$ (where P_b is the binary pe-

riod), corresponding to the orbital period of the innermost region of the circumbinary disk. By contrast, accretion onto eccentric binaries displays larger-amplitude variabilities dominated by pulses with periods of $\sim 1 P_b$ (see Fig. 2).

(2) For equal-mass circular binaries, we find that the accretion rates onto individual stars are quite similar to each other, following an essentially identical accretion pattern in time (Fig. 3, left panels). This result differs from the simulations by Farris et al. (2014), which produced an appreciable disparity between the individual stellar accretion rates. By contrast, we find that accretion onto eccentric binaries exhibits strong symmetry breaking: for a period of time lasting $\sim 200 P_b$ (which corresponds to the apsidal precession period of the innermost region of the circumbinary disk), one of the stars can accrete 10 to 20 times more than the companion (Fig. 3, right panels). This disparity alternates over timescales of $\sim 200 P_b$, such that the long-term accreted masses onto individual stars are the same.

In addition to using a novel moving mesh code (AREPO) that resolves the binary-disk system over a large dynamical range, an important feature of our study is that we carry out our simulations for a sufficiently long time (thousands of binary orbits) and with a proper initial setup. The inner circumbinary disk and the individual circumstellar disks reach a quasi-steady state in which the time-integrated mass accretion is the same across different regions of the system. The ability to reach quasi-steady state gives us confidence that the pulsed accretion behavior uncovered in this paper is not the result of artificial initial conditions.

Our results can be compared to the observations of pulsed accretion in binary T-Tauri stars (BTTS) (Jensen et al. 2007; Muzerolle et al. 2013; Bary & Petersen 2014) and can shed light on the origin of the quasi-periodic variability (in broadband photometry and near-IR line fluxes) observed in these systems. In our simulations, accretion onto eccentric binaries peaks before and during pericenter but never at apocenter. This appears to contradict with the observation of BTTS DQ Tau (with $e_b = 0.56$), which exhibits flaring events during apocenter (Bary & Petersen 2014). This apparent discrepancy can be easily understood once we recognize that the size of the accretion region r_{acc} can strongly affect the measured variability of accretion rates (Section 3.4). In the case of DQ Tau, pericenter passage of the binary (at the separation of $r_p = a_b(1 - e_b) \approx 0.05$ AU; Mathieu et al. 1997) would limit the size of circumstellar disks to be less than $\sim r_p/3 \approx 0.02$ AU, i.e., about 2-3 pre-main-sequence stellar radii, making circumstellar disk accretion irrelevant (especially if the stellar magnetospheres are indeed colliding at periastron; Salter et al. 2010), with accretion proceeding almost directly from the streamers to the stars. In addition, it is possible that the shocked gas responsible for line emission is not strictly confined to the stellar photospheres (Calvet & Gullbring 1998), but located elsewhere in the circumbinary cavity (e.g. Bary & Petersen 2014). Indeed, our eccentric binary simulations do show that shocks appear as material is swung out from the edges of the circumstellar disk at each close passage; this outflowing material meets the inflowing accretion streams from the circumbinary disk. As the disk flow is highly supersonic, the eccentric accretion streams could shock against material at a relative Mach number of $\mathcal{M} \sim 10$. We plan to explore the observational signatures of these shocks in future work.

Finally, although we have focused on accretion onto pre-main sequence binaries in this paper, our simulations also

have implications for accretion onto supermassive binary black holes (SMBBHs). In Section 3.4 we have discussed how the size of the accreting region r_{acc} can affect the variability of accretion rates, such that when $r_{\text{acc}} \rightarrow 0$, modulations of accretion on timescales much shorter than the circumstellar disk viscous time are damped out. Since we expect $r_{\text{acc}} \ll a_b$ for SMBBHs, the individual black holes in a binary would accrete at the nominal supply rate, suppressing fast variability. If this is the case, the mechanism behind the observational hints of photometric variability of SMBBHs would most likely be due to Doppler beaming, as suggested by D’Orazio et al. (2015), rather than to gas dynamics within the circumbinary cavity.

DJM thanks Volker Springel for making AREPO available for use in this work. We thank Ryan Miranda for useful discussions. This work has been supported in part by NSF grant AST-1211061, and NASA grants NNX14AG94G and NNX14AP31G.

REFERENCES

- Andersen, J., Lindgren, H., Hazen, M. L., & Mayor, M. 1989, *A&A*, 219, 142
- Artymowicz, P., & Lubow, S. H. 1996, *ApJ*, 467, L77
- Bary, J. S., Matt, S. P., Skrutskie, M. F., Wilson, J. C., Peterson, D. E., & Nelson, M. J. 2008, *ApJ*, 687, 376
- Bary, J. S., & Petersen, M. S. 2014, *ApJ*, 792, 64
- Basri, G., Johns-Krull, C. M., & Mathieu, R. D. 1997, *AJ*, 114, 781
- Calvet, N., & Gullbring, E. 1998, *ApJ*, 509, 802
- Cuadra, J., Armitage, P. J., Alexander, R. D., & Begelman, M. C. 2009, *MNRAS*, 393, 1423
- Danby, J. M. A. 1988, *Fundamentals of Celestial Mechanics* (Richmond, VA: Willmann-Bell, 1988)
- de Val-Borro, M., Gahm, G. F., Stempels, H. C., & Pepliński, A. 2011, *MNRAS*, 413, 2679
- D’Orazio, D. J., Haiman, Z., & MacFadyen, A. 2013, *MNRAS*, 436, 2997
- D’Orazio, D. J., Haiman, Z., & Schiminovich, D. 2015, *Nature*, 525, 351
- Eggleton, P. P. 1983, *ApJ*, 268, 368
- Farris, B. D., Duffell, P., MacFadyen, A. I., & Haiman, Z. 2014, *ApJ*, 783, 134
- Günther, R., & Kley, W. 2002, *A&A*, 387, 550
- Hanawa, T., Ochi, Y., & Ando, K. 2010, *ApJ*, 708, 485
- Huerta, M., Hartigan, P., & White, R. J. 2005, *AJ*, 129, 985
- Jensen, E. L. N., Dhital, S., Stassun, K. G., Patience, J., Herbst, W., Walter, F. M., Simon, M., & Basri, G. 2007, *AJ*, 134, 241
- Lines, S., Leinhardt, Z. M., Baruteau, C., Paardekooper, S.-J., & Carter, P. J. 2015, *A&A*, 582, A5
- Lynden-Bell, D., & Pringle, J. E. 1974, *MNRAS*, 168, 603
- MacFadyen, A. I., & Milosavljević, M. 2008, *ApJ*, 672, 83
- Mathieu, R. D., Stassun, K., Basri, G., Jensen, E. L. N., Johns-Krull, C. M., Valenti, J. A., & Hartmann, L. W. 1997, *AJ*, 113, 1841
- Miranda, R., & Lai, D. 2015, *MNRAS*, 452, 2396
- Muñoz, D. J., Kratter, K., Springel, V., & Hernquist, L. 2014, *MNRAS*, 445, 3475
- Muñoz, D. J., Kratter, K., Vogelsberger, M., Hernquist, L., & Springel, V. 2015, *MNRAS*, 446, 2010
- Muñoz, D. J., Springel, V., Marcus, R., Vogelsberger, M., & Hernquist, L. 2013, *MNRAS*, 428, 254
- Muzerolle, J., Furlan, E., Flaherty, K., Balog, Z., & Gutermuth, R. 2013, *Nature*, 493, 378
- Pakmor, R., Kromer, M., Taubenberger, S., & Springel, V. 2013, *ApJ*, 770, L8
- Pakmor, R., Springel, V., Bauer, A., Mocz, P., Muñoz, D. J., Ohlmann, S. T., Schaal, K., & Zhu, C. 2016, *MNRAS*, 455, 1134
- Pelupessy, F. I., & Portegies Zwart, S. 2013, *MNRAS*, 429, 895
- Prato, L., Simon, M., Mazeh, T., Zucker, S., & McLean, I. S. 2002, *ApJ*, 579, L99
- Rafikov, R. R. 2016, *ArXiv e-prints*
- Roedig, C., Sesana, A., Dotti, M., Cuadra, J., Amaro-Seoane, P., & Haardt, F. 2012, *A&A*, 545, A127
- Salter, D. M., Kóspál, Á., Getman, K. V., Hogerheijde, M. R., van Kempen, T. A., Carpenter, J. M., Blake, G. A., & Wilner, D. 2010, *A&A*, 521, A32
- Shakura, N. I., & Sunyaev, R. A. 1973, *A&A*, 24, 337
- Shi, J.-M., Krolik, J. H., Lubow, S. H., & Hawley, J. F. 2012, *ApJ*, 749, 118
- Springel, V. 2010, *MNRAS*, 401, 791
- Springel, V., Yoshida, N., & White, S. D. M. 2001, *New Astron.*, 6, 79